Distinguishing between the deep trapping transients of electrons and holes in the microwave response of TiO_2 nanotube arrays

Mohammad H. Zarifi[*]*, Benjamin Wiltshire, Najia Mahdi, Karthik Shankar*[*] *and Mojgan Daneshmand*[*]

Prof. Zarifi, School of Engineering, University of British Columbia, V1V 1V7, Canada
E-mail: mohammad.zarifi@ubc.ca
Prof. K. Shankar, Prof. M. Daneshmand, Department of Electrical and Computer Engineering, University of Alberta, T6G 2V4, Canada
Email: kshankar@ualberta.ca, daneshmand@ualberta.ca
B. D. Wiltshire, N. Mahdi,
Department of Electrical and Computer Engineering, University of Alberta, T6G 2V4, Canada

Abstract

A large signal direct current (DC) bias and a small signal microwave bias were simultaneously applied to TiO_2 nanotube membranes mounted on a planar microwave resonator. The DC bias modulated the electron concentration in the TiO_2 nanotubes, and was varied between 0 and 120 V in this study. Transients immediately following the application and removal of DC bias were measured by monitoring the S-parameters of the resonator as a function of time. The DC bias stimulated Poole-Frenkel type trap-mediated electrical injection of excess carriers into TiO_2 nanotubes which resulted in a near constant resonant frequency but a pronounced decrease in the microwave amplitude due to free electron absorption. When ultraviolet illumination and DC bias were both present and then step-wise removed, the resonant frequency shifted due to trapping - mediated change in the dielectric constant of the nanotube membranes. Characteristic lifetimes of 60-80 s, 300−800 s and ~3000 s were present regardless of whether light or bias was applied and were also observed in the presence of a hole scavenger, which we attributed to oxygen adsorption and deep electron traps while another characteristic lifetime > 8000 s was only present when illumination was applied, and is attributed to the presence of hole traps.

Keywords: carrier dynamics, microwave dielectric properties, photoconductivity, electrochemical anodization, nanotubes

Introduction

Titanium dioxide is a wide bandgap *n*-type semiconductor with versatile optoelectronic applications in dye-sensitized, quantum dot-sensitized and halide perovskite solar cells,[1–6] oxidation and reduction photocatalysts,[7–10] and both ultraviolet and broadband photodetectors.[11,12] The advantages of using TiO_2 nanotubes (TNTs) for sensing are a simple fabrication process, low cost, high active surface area and ease of functionalization, due to which TNTs have been employed in fluorescence-based immunoassays,[13–15] electrochemical sensors for small molecules,[16–18] photoelectrochemical immunoassays[19,20] and chemoresistive sensors for common gases and volatile organic compounds (VOCs).[21–28] In each of the aforementioned applications, the dynamics of charge carriers plays an important role in determining device performance. In this report, we probe long-lived charge separated states using a new methodology.

The TNT architecture formed by electrochemical anodization allows for vectorial charge transport (instead of a random walk)[29–32] and efficient infiltration by high work-function metals and *p*-type semiconductors to form functional heterojunctions.[33–39] At the same time, TNTs are known to suffer from a high concentration of both shallow and deep level traps but very different in distribution from TiO_2 nanoparticle electrodes,[40–46] the understanding of which is key to the optimization of performance in optoelectronic device applications. In this study, we show how to distinguish between the trapping transients of electrons and holes through monitoring the temporal microwave response of TNT membranes.

Planar microwave sensors consisting of coplanar waveguides, transmission lines and ring-type resonators offer distinct advantages for the sensing of semiconductor properties such as high resolution, electrodeless sensing, and real time monitoring.[47–55] Microwave sensing involves measurement and analysis of the interaction of microwave signals with the membrane, film or liquid under test. Microwave resonators are compatible with lab-on-a-chip miniaturization and offer integrated form factors; additionally, research on the preparation of TiO_2 crystal materials with high intensity microwave radiation has shown to be beneficial to electronic properties.[56–58] The authors introduced integrated planar radio frequency (RF) resonators for the characterization and analysis of the electronic behavior of TiO_2 nanotubes.[46] It has been shown that utilizing planar RF resonators, one can obtain detailed information through analysis of the steady state or time resolved photoconductivity response. This technique has been used to obtain better understanding of the surface functionalization of TiO_2 nanotubes and their interaction with the surrounding medium.[59] In this report, it is shown that the application of a DC bias superimposed on the small signal microwave stimulation enables an amplification of the microwave conductivity response of TiO_2 nanotube arrays while the frequency of the sensing platform stays stable. The similarities and differences in the time-resolved microwave spectra of TNT arrays subjected to different values of DC bias with and without the simultaneous application of optical bias allow us to deduce information regarding trapping and recombination processes in the nanotubes. These results provide important insights for the design and optimization of higher performance TNT-based photocatalysts, photovoltaics and photodetectors.

A microstrip planar ring resonator device was designed and simulated to operate at 2.61 GHz with a quality factor of 250. The designed resonator was customized to deliver DC voltages between the resonant ring and one of its signal lines across the coupling gap. A microstrip line

with an electrical length of λ/4 was designed and connected to the main ring structure to deliver the required bias voltages. The DC-feed line was grounded on its other end using a capacitor and was considered as a high impedance load from the resonator side. Two bias tees were also considered in the input and output of the resonator device. These components had no significant effect on the high-frequency operation of the device but were necessary to establish the required circuitry for the DC voltages across the coupling gap (**Figure 1a**) and ensure isolation between the device and the measurement ports. The simulation results for the designed structure demonstrated a 3 dB quality factor of 250 at the resonance frequency of 2.61 GHz with a resonant amplitude of -13.17 dB. Since the quality factor (Q) and the resolution of the ring resonator sensor for minimum detectable permittivity sensing are inversely related ($\Delta\varepsilon \propto Q^{-1}$), having a high quality factor leads to a ring resonator device with high resolution.[50]

The surface magnetic current was studied in simulation in order to confirm the negligible effect of the DC-feed line on the resonant ring. As shown in **Figure 1b**, the maximum magnetic current flow was across the input and output microwave ports, and the microstrip line feeding the DC bias had a negligible loading effect on the resonant circuitry. The resonant profile of the simulated structure (obtained using Ansys HFSS) and measured profile are presented and compared in **Figure 1c**, where an acceptable level of agreement between the measured and the simulation results can be observed. The difference between these two profiles can be justified considering the soldering effect from connectors, and variation in parameters during the implementation process of the microwave circuitry. The designed structure demonstrated more sensitivity to the variation in dielectric properties in select regions where the electric field had a larger value than the other regions. The electric field distribution on a plane 0.1 mm above the resonator substrate is presented in **Figure 1d**. The coupling gap areas, between the signal lines and

the ring microstrip line, demonstrated larger electric field distribution in comparison to the other places, which were used as a sensitive location for mounting the TiO_2 nanotube membrane sample.

Titanium foils with a thickness of 0.89 mm (99.7%, Alfa Aesar) were degreased by sonication in methanol for 10 minutes, rinsed with water and then dried in a stream of flowing, pressurized nitrogen. Electrochemical anodization was performed using pieces of Ti foil as both the anode and cathode with an inter-electrode distance of 3 cm. The areas of the Ti anode and cathode were 1 x 4 cm and 0.5 x 4 cm respectively. ~ 100 μm-long TiO_2 nanotubes were anodically formed over three days using an anodization voltage of 60 V. An ethylene glycol-based organic electrolyte with 0.3 wt % NH_4F and 4 vol % DI water was used as the electrolyte. The edges of the as-prepared TNTs on foil were first scratched and then rinsed with both methanol and water to obtain free-standing, amorphous TNT membranes which were subsequently subjected to a crystallizing anneal at 350° C for 20 hours. The morphology of annealed TNTs was observed using a field emission scanning electron microscope (FESEM; Hitachi S-4800) with an accelerating voltage of 5 kV and a filament current of 20 μA, (**Figure 2**). The crystallinity of annealed TNTs was investigated by an X-ray diffractometer (Bruker D8 Discover) (not shown).

The resonator was fabricated on a RF substrate 5880 from Rogers Corporation. The substrate has a permittivity of 2.2 and dielectric thickness of 0.79 mm. A copper layer on the top and bottom surface of the substrate with a thickness of 0.035 mm, was used to implement the microstrip lines and the ground layer beneath them. The TNT membrane was placed in the coupling gap between the signal line and the ring structure and was electrically connected to the copper microstrips with conductive silver paste. Two bias Tees were used to establish a bias voltage to ground path, and an isolation protection to the measurement instrument in port 1 and 2. A vector network analyzer (VNA) from National Instruments Corp. with embedded Labview software was used to measure

the scattering parameter (S_{21}), which represents the transmission coefficient of microwaves incident at the input port of the resonator. The S_{21} parameter was measured with sampling period of 10 second.

The output power at the VNA port was 5 dBm and the intermediate frequency (IF) bandwidth was set to 1 kHz. The DC bias voltage was provided by a λ/4 microstrip line which was directly connected to the ring resonator loop. This bias line was considered as a high impedance (open-load) in the operating frequency range (2.4-2.5 GHz) of the sensor. An ultraviolet (UV) lamp with a centre wavelength of 254 nm was located at a distance of 15 cm from the top surface of the resonator and the attached membrane and the environmental parameters such as temperature and humidity were kept constant during the experiments at 23˚C and 32 %, respectively.

We used free-standing TNT membranes with a thickness of ~ 115 μm. The microwave response of such membranes can be probed in at least two different ways as shown in **Figure 3**. The electronic bandgap of anatase phase TiO_2 is 3.2 eV and anatase has an absorption coefficient $\alpha > 5 \times 10^4$ cm^{-1} for photons with energies significantly larger than 3.2 eV.[60] The penetration depth of incident photons is given by $L_p = 1/\alpha$, which is < 200 nm in the TNTs for 254 nm ultraviolet radiation. In the configuration shown in **Figure 3a**, the extremely thin photoexcited top layer is capacitively coupled to the coupling gap of the microwave resonator. Such a configuration is not able to sensitively detect changes in the membrane conductivity from the ultraviolet illumination due to the large series resistance of the non-excited portion of the membrane but is nevertheless able to detect fairly small changes in the dielectric constant of the TNT membrane due to photoexcitation. On the other hand, in the configuration shown in **Figure 3b**, silver paint is used to make a direct electrical contact from the microstrips to the illuminated top surface of the TNT membrane, and is far more sensitive to changes in the conductivity of the TNT membrane close to

its top surface at the expense. Thus, the first configuration is valuable for purely probing the photodielectric effect while in the second configuration, the photoconductivity impact shows more significantly. The configuration shown in **Figure 3b** was used in this report, and a photograph of the experimental setup showing the microwave ring resonator sensor, TNT membrane and bias Tee is presented in **Figure S1**.

S_{21} parameters were measured as a function of time with and without the application of a DC bias. The resonant profile is presented in **Figure 4a**, which has a maximum amplitude (resonant amplitude) at the resonance frequency. The resonant amplitude and frequency are the two main characteristics of the sensor and were monitored in the experiments. **Figure 4b** presents the resonant amplitude variation for bias voltage of 80 V for a 5-minute duration. Results for this experiment were obtained in the dark with no UV illumination of the nanotube membrane. According to the recorded results, the application of the DC bias voltage decreased the resonant amplitude while having no effect on the resonance frequency (**Figures 4c and 4d**). This is a confirmation that by application of the DC bias voltage, conductivity of the nanotube membrane varies while permittivity remains relatively unchanged.

Table 1. The microwave responses of TiO_2 nanotube membranes for different values of DC bias fitted to biexponential decays.

	V_{DC}=120 (V)	V_{DC}=100	V_{DC}=80	V_{DC}=60	V_{DC}=40	V_{DC}=20	Voltage Status
y_0 (dB)	-19.17	-19.18	-19.06	-18.85	-18.80	-18.77	
A_1 (dB)	0.267	0.276	0.184	0.047	0.023	0.008	
T_1 (sec)	106.09	599.15	918.12	317.78	315.22	150.82	
A_2 (dB)	0.117	0.052	0.002	-	-	-	
T_2 (sec)	11.06	55.91	66.86	-	-	-	
ΔA_{res} (dB)	0.363	0.207	0.088	0.036	0.016	0.008	

X_r^2	9.0×10^{-6}	8.6×10^{-6}	2.2×10^{-6}	3.8×10^{-6}	2.3×10^{-6}	2.9×10^{-6}	ON
R^2	0.998	0.998	0.996	0.961	0.904	0.631	
y_0' (dB)	-18.84	-18.84	-18.81	-18.77	-18.76	-18.73	OFF
B_1 (dB)	-0.240	-0.133	-0.077	-0.053	-0.026	-0.022	
T_1'(sec)	3084.54	3476.43	2958.98	3020.68	3335.59	11134.22	
B_2 (dB)	-0.004	-0.003	-0.004	-	-	-	
T_2' (sec)	106.70	135.99	102.02	-	-	-	
X_r^2	1.7×10^{-5}	3.1×10^{-6}	2.0×10^{-6}	1.8×10^{-6}	1.9×10^{-6}	2.1×10^{-6}	
R^2	0.995	0.998	0.994	0.987	0.950	0.770	

A comparison between the resonant amplitude variation for different DC bias voltages is presented in **Figure 4d**. According to these results, the amplitude and decay time constants are the two main parameters that changed for different voltage levels. Moreover, no significant change in the resonant frequency was observed during the period when the DC voltages were applied across the nanotube membrane sample. The resonant amplitude decays versus time during the DC bias excitation were fit to a biexponential decay function ($y = y_0 + A_1 e^{-t/T_1} + A_2 e^{-t/T_2}$) consisting of a fast component (T_2, ON) in the tens of seconds and a slower component (T_1, ON) in the hundreds of seconds (Table 1). Both components became shorter-lived (decay constants decreased in magnitude) as the bias value increased. For the smaller values of DC bias, the faster and slower components could not be resolved. The faster component is consistent with the migration of electrons to the surface followed by capture by oxygen to form adsorbed oxide.[61,62] The slower component can be understood in the context of the deep trap-mediated injection of excess electrons from the contacts. Such injection involves the emission of trapped electrons shown in **Figure 5** albeit with a reduction in the thermal energy required by a trapped carrier to escape due to the

applied electric field (Poole-Frenkel effect). The resulting mobile excess electrons absorb microwaves and generate transmission losses in the resonator circuit similar to the losses produced by a conductive substrate. The decay constant is an indirect measure of the activation energy barrier encountered by trapped electrons. Greater the activation barrier, longer the decay constants.[63] Since the electric field across the membrane produced by higher DC bias values reduces the effective activation energy barrier, the corresponding time constants for the emission of electrons from deep traps also decrease (**Table 1** and **Figure 4d**). Multiple reports have established an energetic depth of 1.0-1.4 eV for deep electron traps in anatase-phase TiO_2 nanotubes;[44,46,64,65] this energy barrier is reduced to 0.85-0.95 eV for a lateral membrane bias of 120 V per our results.

When the DC bias is removed, the amplitude of the microwave signal recovers to its pre-illumination values over a period of several hours. A bi-exponential decay function ($y' = y_0' + B_1 e^{-t/T_1'} + B_2 e^{-t/T_2'}$) was used as a fitting function for the recovery period after the removal of the DC bias. The parameters of the fitting functions for different bias voltages are reported and compared in Table 1. In this case, the time constants consisted of a slow component (T_1') of ~ 3000 s and a fast component (T_2') of ~ 100 s, and were found to be relatively independent of applied bias. For low values of bias, the faster component was not detected. While the DC bias is applied, the deep traps releasing electrons are quickly re-filled by electrons injected from the contacts. Consequently, the number of bound charges remains constant which manifests itself in a near-constant resonant frequency (**Figure 4c**). When the DC bias is disconnected, contact injection ceases but the excess electrons in the conduction band of the TiO_2 nanotubes can no longer decay to the previous trap levels that are now filled. The electrons decay instead to a different type of trap site which has a much smaller capture cross-section resulting in slow re-trapping which is

evidenced by the several hour-long relaxation of the perturbation in the microwave response (**Figure 4d**) following the removal of the DC bias.

The effect of DC bias voltages on carrier dynamics in the titania nanotube membranes was also studied in the presence of UV light. To ensure a stable DC connection between the sample and the ring resonator device, the resistance variation was observed using a Keithley 2100 digital multimeter. According to the presented results in **Figure 6a** during the UV-light illumination, the resistance drops from 110 MΩ to 30 MΩ. The resistance variation profile demonstrated a good fitting with $R(t) = R_0 + R_1 e^{-(t-t_0)/T1} + R_2 e^{-(t-t_0)/T2}$, function, while the microwave amplitude response (**Figure 6b**) could be fitted to $R(t) = R_0 + R_1 e^{-(t-t_0)/T1} + R_2 e^{-(t-t_0)/T2} + R_3 e^{-(t-t_0)/T3}$. The parameters of the fitting functions are provided in **Table 2**. When both ultraviolet (UV) illumination and a DC bias are applied, the resulting decays of the microwave amplitude (corresponds to a photoconductivity rise time) exhibit some interesting similarities and differences to the case when DC bias alone is applied. On the one hand, the time constants for the amplitude decay are very similar in the presence of UV illumination and consist of a slow component with a time constant of 300−800 s and a faster component in the range 55−85 s (**Figure 6b** and **Table S1**). On the other hand, there is a clear bias-independent shift in the resonance frequency due to UV illumination (**Figure 6d**), which indicates an increase in the number of bound charges due to trap filling. Furthermore, the amplitudes of the microwave decays range from 0.5-1.1 dB in the presence of UV illumination (**Figure 6c** and **Table S1**) as contrasted with a range of 0.008 - 0.36 dB in the presence of DC bias alone. Taken together, the results indicate that the microwave photoconductance of the TiO_2 nanotubes in the presence of combined UV illumination and DC bias is dominated by the majority carrier Poole-Frenkel effect as in the case of pure DC bias but that carrier trapping is significant for UV photoexcitation and contributes to a shift in the resonant

frequency through the photodielectric effect. The results also indicate that the number of excess carriers produced by illumination is vastly greater than the number of excess carriers produced by the application of DC bias alone.

Table 2. Fitness functions parameters for regeneration and relaxation response for resistance measurement

	R_0	R_1	R_2	R_3	t_0	T_1	T_2	T_3	COD (R^2)	Chi^2
Regeneration	-3.85e11	6.03e7	3.86e11	0	120	26.24	8.107e7	0	0.994	1.5e12
Relaxation	1.1e8	-7.48e6	-2.04e7	-5.23e7	420	12.34	141.52	2319	0.998	1.7e11

After the UV illumination is switched off, we observed two distinct transient behaviors corresponding to when the DC bias was still present and when the DC bias was subsequently disconnected. The lifetime component in the UV relaxation response of the resonators while the DC bias is still applied reveals a lifetime component at ~ 3000 s which is observed in the recovery following the application of DC bias, and also in the presence of hole scavengers studied in our previous work.[66] This is most likely due to low capture cross-section deep electron traps at the surface that do not experience the field-mediated reduction of energy barriers due to the countervailing built-in field at the surface due to adsorbed oxide ions. When both the DC bias and the UV illumination are switched off, the recovery of the microwave response back to equilibrium is dominated by longer lived components (time constants > 8000 s) as seen in **Table S1**, which we assign to the emission of holes from deep level trap states and subsequent fast recombination with majority carrier electrons. This assignment is provided support from the disappearance of this long-lived component from the recovery transients following UV illumination in the presence of short chain aliphatic alcohols which scavenge trapped holes.[63] The effect of humidity was reported in our previous work;[67] humidity can compete with oxygen to trap electrons, and in addition water

molecules adsorbed on defect sites present in superhydrophilic TiO_2 nanotubes can be chemically dissociated resulting in proton intercalation into the TiO_2, thus increasing conductivity.

The objectives of this study were two-fold - firstly to better understand the dynamics of trapping in anodic titania nanotubes from the viewpoint of improving device performance in nanotube-based photodetectors, photocatalysts and solar cells. Secondly, an emerging paradigm refuses to consider carrier trapping to be a purely negative phenomenon and recognizes the utility of trap states in high selectivity sensing and catalysis given optimal design and understanding. TiO_2 nanotubes annealed at 350 °C exhibit the maximum microwave response unlike say nanotubes annealed at 500° C, which is beneficial for both the aforementioned objectives. A 350°C oxygen anneal converts the bulk of the TiO_2 nanotubes to the anatase phase but still leaves some amorphous uncrystallized TiO_2 domains and remnant interstitial fluoride species from the anodization process, which are the likely sources of the dominant electron traps observed in this study. An applied DC bias at symmetrical Ag contacts with a work function well-matched to anatase TiO_2 can only produce conduction due to majority carriers. Minority carriers are negligible in *n*-type TiO_2 nanotubes and therefore minority carrier recombination plays no role in the microwave response transients produced by the application and removal of a DC bias. When ultraviolet illumination is applied by itself (DC bias = 0 V) or together with a finite DC bias of 20−120 V, the behavior of minority carriers can no longer be ignored while considering the corresponding transients. From a characterization perspective, this report demonstrates the ability to separately resolve majority- and minority-carrier trapping transients by simultaneously applying a DC bias while probing the temporal responses of the microwave conductance and photoconductance.

Conclusion

In this report, the impact of DC bias on the microwave conductivity and photoconductivity of anatase-phase TiO_2 nanotube membranes was monitored in the time-domain using a planar ring-type microwave resonator operating at 2.45 GHz. Through the application of a DC bias in conjunction with bandgap illumination followed by their stepwise removal, one obtains richer insights into the underlying carrier dynamics, and can also distinguish between the trapping transients due to majority and minority carriers. Furthermore, planar resonator measurement configurations capable of sensitively probing both the photodielectric effect and the photoconductivity effect are shown. High surface area anodically formed titania nanotube membranes annealed at 350 °C produce a near-constant and unchanging resonant frequency in their microwave response following the application and removal of a DC bias, thus not exhibiting the expected change in the dielectric constant due to the creation of bound charges from trap filling. When UV illumination was applied together with a DC bias, the resonant frequency exhibited a noticeable shift indicative of trap filling. However, the photoconductivity rise times of tens and hundreds of seconds in the microwave amplitude response strongly indicated the involvement of deep trap states. We attribute the slow rise in the photoconductivity to electron capture by oxygen at the surface and also to Poole-Frenkel type trap-mediated injection from the contacts. The bias-independent photoconductivity decay time constant of ~ 3000 s following the removal of the DC bias was attributed to the capture of electrons into lower cross-section deep trapping states at the surface. Hole trapping transients with minimum lifetimes of 8000 s were seen purely in the recovery response of nanotube membranes subjected to UV illumination with no applied bias present.

Supporting Information. Images and description of the experimental setup. Fitness function parameters for all experiments.

Acknowledgements

All authors thank NSERC and Canada Research Chair Program for financial support. Support toward equipment usage from NRC-NINT and CMC Microsystems is gratefully acknowledged.

B.D.W. and S.F. acknowledge scholarship support from Alberta Innovates Technology Futures.

Received: ((will be filled in by the editorial staff))
Revised: ((will be filled in by the editorial staff))
Published online: ((will be filled in by the editorial staff))

References

(1) Varghese, O. K.; Paulose, M.; Grimes, C. A. Long Vertically Aligned Titania Nanotubes on Transparent Conducting Oxide for Highly Efficient Solar Cells. *Nat. Nanotechnol.* **2009**, *4* (9), 592–597.

(2) Shankar, K.; Mor, G. K.; Paulose, M.; Varghese, O. K.; Grimes, C. A. Effect of Device Geometry on the Performance of TiO2 Nanotube Array-Organic Semiconductor Double Heterojunction Solar Cells. *J. Non. Cryst. Solids* **2008**, *354* (19–25), 2767–2771.

(3) Tao, L.; Xiong, Y.; Liu, H.; Shen, W. High Performance PbS Quantum Dot Sensitized Solar Cells via Electric Field Assisted in Situ Chemical Deposition on Modulated TiO_2 Nanotube Arrays. *Nanoscale* **2014**, *6* (2), 931–938.

(4) Qin, P.; Paulose, M.; Dar, M. I.; Moehl, T.; Arora, N.; Gao, P.; Varghese, O. K.; Grätzel, M.; Nazeeruddin, M. K. Stable and Efficient Perovskite Solar Cells Based on Titania Nanotube Arrays. *Small* **2015**, *11* (41), 5533–5539.

(5) Bandara, J.; Shankar, K.; Basham, J.; Wietasch, H.; Paulose, M.; Varghese, O. K.; Grimes, C. A.; Thelakkat, M. Integration of TiO_2 Nanotube Arrays into Solid-State Dye-Sensitized Solar Cells. *Eur. Phys. J. Appl. Phys.* **2011**, *53* (2), 20601.

(6) Thakur, U. K.; Askar, A. M.; Kisslinger, R.; Wiltshire, B. D.; Kar, P.; Shankar, K. Halide Perovskite Solar Cells Using Monocrystalline TiO_2 Nanorod Arrays as Electron Transport Layers: Impact of Nanorod Morphology. *Nanotechnology* **2017**, *28* (27), 274001.

(7) Liu, N.; Häublein, V.; Zhou, X.; Venkatesan, U.; Hartmann, M.; Mačković, M.; Nakajima, T.; Spiecker, E.; Osvet, A.; Frey, L.; et al. "Black" TiO_2 Nanotubes Formed by High-Energy Proton Implantation Show Noble-Metal- *Co* -Catalyst Free Photocatalytic H_2 -Evolution. *Nano Lett.* **2015**, *15* (10), 6815–6820.

(8) Weon, S.; Choi, W. TiO_2 Nanotubes with Open Channels as Deactivation-Resistant Photocatalyst

for the Degradation of Volatile Organic Compounds. *Environ. Sci. Technol.* **2016**, *50* (5), 2556–2563.

(9) Kang, Q.; Wang, T.; Li, P.; Liu, L.; Chang, K.; Li, M.; Ye, J. Photocatalytic Reduction of Carbon Dioxide by Hydrous Hydrazine over Au-Cu Alloy Nanoparticles Supported on $SrTiO_3$/TiO_2 Coaxial Nanotube Arrays. *Angew. Chemie Int. Ed.* **2015**, *54* (3), 841–845.

(10) Kar, P.; Farsinezhad, S.; Mahdi, N.; Zhang, Y.; Obuekwe, U.; Sharma, H.; Shen, J.; Semagina, N.; Shankar, K. Enhanced CH4 Yield by Photocatalytic CO2 Reduction Using TiO2 Nanotube Arrays Grafted with Au, Ru, and ZnPd Nanoparticles. *Nano Res.* **2016**, *9* (11), 3478–3493.

(11) Zou, J.; Zhang, Q.; Huang, K.; Marzari, N. Ultraviolet Photodetectors Based on Anodic TiO_2 Nanotube Arrays. *J. Phys. Chem. C* **2010**, *114* (24), 10725–10729.

(12) Zheng, L.; Hu, K.; Teng, F.; Fang, X. Novel UV-Visible Photodetector in Photovoltaic Mode with Fast Response and Ultrahigh Photosensitivity Employing Se/TiO_2 Nanotubes Heterojunction. *Small* **2017**, *13* (5), 1602448.

(13) Song, Y.-Y.; Schmidt-Stein, F.; Berger, S.; Schmuki, P. TiO2 Nano Test Tubes as a Self-Cleaning Platform for High-Sensitivity Immunoassays. *Small* **2010**, *6* (11), 1180–1184.

(14) Kar, P.; Pandey, A.; Greer, J. J.; Shankar, K. Ultrahigh Sensitivity Assays for Human Cardiac Troponin I Using TiO2 Nanotube Arrays. *Lab Chip* **2012**, *12* (4), 821-828.

(15) Farsinezhad, S.; Mohammadpour, A.; Dalrymple, A. N.; Geisinger, J.; Kar, P.; Brett, M. J.; Shankar, K. Transparent Anodic TiO₂ Nanotube Arrays on Plastic Substrates for Disposable Biosensors and Flexible Electronics. *J. Nanosci. Nanotechnol.* **2013**, *13* (4), 2885–2891.

(16) Wang, C.; Yin, L.; Zhang, L.; Gao, R. Ti/TiO_2 Nanotube Array/Ni Composite Electrodes for Nonenzymatic Amperometric Glucose Sensing. *J. Phys. Chem. C* **2010**, *114* (10), 4408–4413.

(17) Hu, L.; Huo, K.; Chen, R.; Gao, B.; Fu, J.; Chu, P. K. Recyclable and High-Sensitivity Electrochemical Biosensing Platform Composed of Carbon-Doped TiO_2 Nanotube Arrays. *Anal. Chem.* **2011**, *83* (21), 8138–8144.

(18) Kar, P.; Shankar, K. Biodiagnostics Using Oriented and Aligned Inorganic Semiconductor Nanotubes and Nanowires. *J. Nanosci. Nanotechnol.* **2013**, *13* (7), 4473–4496.

(19) An, Y.; Tang, L.; Jiang, X.; Chen, H.; Yang, M.; Jin, L.; Zhang, S.; Wang, C.; Zhang, W. A Photoelectrochemical Immunosensor Based on Au-Doped TiO2 Nanotube Arrays for the Detection of α-Synuclein. *Chem. - A Eur. J.* **2010**, *16* (48), 14439–14446.

(20) Zhao, W.-W.; Ma, Z.-Y.; Yan, D.-Y.; Xu, J.-J.; Chen, H.-Y. *In Situ* Enzymatic Ascorbic Acid Production as Electron Donor for CdS Quantum Dots Equipped TiO_2 Nanotubes: A General and Efficient Approach for New Photoelectrochemical Immunoassay. *Anal. Chem.* **2012**, *84* (24), 10518–10521.

(21) Yoriya, S.; Prakasam, H. E.; Varghese, O. K.; Shankar, K.; Paulose, M.; Mor, G. K.; Latempa, T. J.; Grimes, C. A. Initial Studies on the Hydrogen Gas Sensing Properties of Highly-Ordered High Aspect Ratio TiO₂ Nanotube-Arrays 20 <I>µ</I>m to 222 <I>µ</I>m in Length. *Sens. Lett.* **2006**, *4* (3), 334–339.

(22) Lin, S.; Li, D.; Wu, J.; Li, X.; Akbar, S. A. A Selective Room Temperature Formaldehyde Gas Sensor Using TiO2 Nanotube Arrays. *Sensors Actuators B Chem.* **2011**, *156* (2), 505–509.

(23) Rao, B. M.; Roy, S. C. Solvothermal Processing of Amorphous TiO_2 Nanotube Arrays: Achieving Crystallinity at a Lower Thermal Budget. *J. Phys. Chem. C* **2014**, *118* (2), 1198–1205.

(24) Lu, H. F.; Li, F.; Liu, G.; Chen, Z.-G.; Wang, D.-W.; Fang, H.-T.; Lu, G. Q.; Jiang, Z. H.; Cheng, H.-M. Amorphous TiO_2 Nanotube Arrays for Low-Temperature Oxygen Sensors. *Nanotechnology* **2008**, *19* (40), 405504.

(25) Zhang, X.; Zhang, J.; Jia, Y.; Xiao, P.; Tang, J. TiO2 Nanotube Array Sensor for Detecting the SF6 Decomposition Product SO2. *Sensors* **2012**, *12* (12), 3302–3313.

(26) Hazra, A.; Dutta, K.; Bhowmik, B.; Chattopadhyay, P. P.; Bhattacharyya, P. Room Temperature Alcohol Sensing by Oxygen Vacancy Controlled TiO_2 Nanotube Array. *Appl. Phys. Lett.* **2014**, *105* (8), 81604.

(27) Lü, R.; Zhou, W.; Shi, K.; Yang, Y.; Wang, L.; Pan, K.; Tian, C.; Ren, Z.; Fu, H. Alumina Decorated TiO2 Nanotubes with Ordered Mesoporous Walls as High Sensitivity NOx Gas Sensors at Room Temperature. *Nanoscale* **2013**, *5* (18), 8569-8576.

(28) Alivov, Y.; Singh, V.; Ding, Y.; Nagpal, P. Transparent Conducting Oxide Nanotubes. *Nanotechnology* **2014**, *25* (38), 385202.

(29) Kai Zhu; Nathan R. Neale; Alexander Miedaner, and; Frank*, A. J. Enhanced Charge-Collection Efficiencies and Light Scattering in Dye-Sensitized Solar Cells Using Oriented TiO2 Nanotubes Arrays. **2006,** 7(1), 69-74.

(30) Choi, J.; Song, S.; Kang, G.; Park, T. Dye-Sensitized Solar Cells Employing Doubly or Singly Open-Ended TiO_2 Nanotube Arrays: Structural Geometry and Charge Transport. *ACS Appl. Mater. Interfaces* **2014**, *6* (17), 15388–15394.

(31) Mohammadpour, A.; Kar, P.; D. Wiltshire, B.; M. Askar, A.; Shankar, K. Electron Transport, Trapping and Recombination in Anodic TiO2 Nanotube Arrays, *Curr. Nanoscience* **2015**, 11(5), 593-614.

(32) *Electrochemically Engineered Nanoporous Materials*; Losic, D., Santos, A., Eds.; Springer Series in Materials Science; Springer International Publishing: Cham, 2015; Vol. 220.

(33) Kim, S.; Mor, G. K.; Paulose, M.; Varghese, O. K.; Shankar, K.; Grimes, C. A. Broad Spectrum Light Harvesting in TiO$_2$ Nanotube Array – Hemicyanine Dye – P3HT Hybrid Solid-State Solar Cells. *IEEE J. Sel. Top. Quantum Electron.* **2010**, *16* (6), 1573–1580.

(34) Assaud, L.; Heresanu, V. Fabrication of P/n Heterojunctions by Electrochemical Deposition of Cu2O onto TiO2 Nanotubes. *Comptes Rendus Chim.* **2013**, *16* (1), 89–95.

(35) Farsinezhad, S.; Sharma, H.; Shankar, K. Interfacial Band Alignment for Photocatalytic Charge Separation in TiO_2 Nanotube Arrays Coated with CuPt Nanoparticles. *Phys. Chem. Chem. Phys.* **2015**, *17* (44), 29723–29733.

(36) Yang, D.; Sun, Y.; Tong, Z.; Tian, Y.; Li, Y.; Jiang, Z. Synthesis of Ag/TiO_2 Nanotube Heterojunction with Improved Visible-Light Photocatalytic Performance Inspired by Bioadhesion. *J. Phys. Chem. C* **2015**, *119* (11), 5827–5835.

(37) Wang, R.; Bai, J.; Li, Y.; Zeng, Q.; Li, J.; Zhou, B. BiVO4/TiO2(N2) Nanotubes Heterojunction Photoanode for Highly Efficient Photoelectrocatalytic Applications. *Nano-Micro Lett.* **2017**, *9* (2),

14.

(38) Yang, T.; Liu, W.; Li, L.; Chen, J.; Hou, X.; Chou, K.-C. Synergizing the Multiple Plasmon Resonance Coupling and Quantum Effects to Obtain Enhanced SERS and PEC Performance Simultaneously on a Noble Metal–semiconductor Substrate. *Nanoscale* **2017**, *9* (6), 2376–2384.

(39) Das, S.; Sopha, H.; Krbal, M.; Zazpe, R.; Podzemna, V.; Prikryl, J.; Macak, J. M. Electrochemical Infilling of $CuInSe_2$ within TiO_2 Nanotube Layers and Subsequent Photoelectrochemical Studies. *ChemElectroChem* **2017**, *4* (3), 495–499.

(40) Jennings, J. R.; Ghicov, A.; Peter, L. M.; Schmuki, P.; Walker, A. B. Dye-Sensitized Solar Cells Based on Oriented TiO_2 Nanotube Arrays: Transport, Trapping, and Transfer of Electrons. *J. Am. Chem. Soc.* **2008**, *130* (40), 13364–13372.

(41) Mohammadpour, R.; Iraji zad, A.; Hagfeldt, A.; Boschloo, G. Comparison of Trap-State Distribution and Carrier Transport in Nanotubular and Nanoparticulate TiO2 Electrodes for Dye-Sensitized Solar Cells. *ChemPhysChem* **2010**, *11* (10), 2140–2145.

(42) Richter, C.; Schmuttenmaer, C. A. Exciton-like Trap States Limit Electron Mobility in TiO2 Nanotubes. *Nat. Nanotechnol.* **2010**, *5* (11), 769–772.

(43) Mercado, C. C.; Knorr, F. J.; McHale, J. L. Observation of Charge Transport in Single Titanium Dioxide Nanotubes by Micro-Photoluminescence Imaging and Spectroscopy. *ACS Nano* **2012**, *6* (8), 7270–7280.

(44) Mercado, C. C.; Knorr, F. J.; McHale, J. L.; Usmani, S. M.; Ichimura, A. S.; Saraf, L. V. Location of Hole and Electron Traps on Nanocrystalline Anatase TiO_2. *J. Phys. Chem. C* **2012**, *116* (19), 10796–10804.

(45) Zhang, Q.; Celorrio, V.; Bradley, K.; Eisner, F.; Cherns, D.; Yan, W.; Fermín, D. J. Density of Deep Trap States in Oriented TiO_2 Nanotube Arrays. *J. Phys. Chem. C* **2014**, *118* (31), 18207–18213.

(46) Zarifi, M. H.; Mohammadpour, A.; Farsinezhad, S.; Wiltshire, B. D.; Nosrati, M.; Askar, A. M.; Daneshmand, M.; Shankar, K. Time-Resolved Microwave Photoconductivity (TRMC) Using Planar Microwave Resonators: Application to the Study of Long-Lived Charge Pairs in Photoexcited Titania Nanotube Arrays. *J. Phys. Chem. C* **2015**, 119(25), 14358-14365.

(47) Perticaroli, S.; Varlamava, V.; Palma, F. Microwave Sensing of Nanostructured Semiconductor Surfaces. *Appl. Phys. Lett.* **2014**, *104* (1), 13110.

(48) Sohrabi, A.; Mojir Shaibani, P.; Zarifi, M. H.; Daneshmand, M.; Thundat, T. A Novel Technique for Rapid Vapor Detection Using Swelling Polymer Covered Microstrip Ring Resonator. In *2014 IEEE MTT-S International Microwave Symposium (IMS2014)*; IEEE, **2014**; pp 1–4.

(49) Zarifi, M. H.; Farsinezhad, S.; Shankar, K.; Daneshmand, M. Liquid Sensing Using Active Feedback Assisted Planar Microwave Resonator. *IEEE Microw. Wirel. Components Lett.* **2015**, *25* (9), 621–623.

(50) Zarifi, M. H.; Thundat, T.; Daneshmand, M. High Resolution Microwave Microstrip Resonator for Sensing Applications. *Sensors Actuators A Phys.* **2015**, *233*, 224–230.

(51) Adhikari, K. K.; Kim, N.-Y. Ultrahigh-Sensitivity Mediator-Free Biosensor Based on a Microfabricated Microwave Resonator for the Detection of Micromolar Glucose Concentrations.

IEEE Trans. Microw. Theory Tech. **2016**, *64* (1), 319–327.

(52) Ali, M. A.; Mark Ming-Cheng Cheng; Jimmy Ching-Ming Chen; Wu, C.-T. M. Microwave Gas Sensor Based on Graphene-Loaded Substrate Integrated Waveguide Cavity Resonator. In *2016 IEEE MTT-S International Microwave Symposium (IMS)*; IEEE, 2016; pp 1–4.

(53) Su, L.; Naqui, J.; Mata-Contreras, J.; Martin, F. Cascaded Splitter/combiner Microstrip Sections Loaded with Complementary Split Ring Resonators (CSRRs): Modeling, Analysis and Applications. In *2016 IEEE MTT-S International Microwave Symposium (IMS)*; IEEE, 2016; pp 1–4.

(54) Zarifi, M. H.; Rahimi, M.; Daneshmand, M.; Thundat, T. Microwave Ring Resonator-Based Non-Contact Interface Sensor for Oil Sands Applications. *Sensors Actuators B Chem.* **2016**, *224*, 632–639.

(55) Mata-Contreras, J.; Herrojo, C.; Martin, F. Application of Split Ring Resonator (SRR) Loaded Transmission Lines to the Design of Angular Displacement and Velocity Sensors for Space Applications. *IEEE Trans. Microw. Theory Tech.* **2017**, *65* (11), 4450–4460.

(56) Tian, F.; Wu, Z.; Chen, Q.; Yan, Y.; Cravotto, G.; Wu, Z. Microwave-Induced Crystallization of AC/TiO2 for Improving the Performance of Rhodamine B Dye Degradation. *Appl. Surf. Sci.* **2015**, *351*, 104–112.

(57) Tian, F.; Wu, Z.; Tong, Y.; Wu, Z.; Cravotto, G. Microwave-Assisted Synthesis of Carbon-Based (N, Fe)-Codoped TiO2 for the Photocatalytic Degradation of Formaldehyde. *Nanoscale Res. Lett.* **2015**, *10* (1), 360.

(58) Tian, F.; Wu, Z.; Yan, Y.; Ye, B.-C.; Liu, D. Synthesis of Visible-Light-Responsive Cu and N-Codoped AC/TiO2 Photocatalyst Through Microwave Irradiation. *Nanoscale Res. Lett.* **2016**, *11* (1), 292.

(59) Zarifi, M. H.; Wiltshire, B.; Mahdi, N.; Kar, P.; Shankar, K.; Daneshmand, M. Ultraviolet Sensing Using a TiO_2 Nanotube Integrated High Resolution Planar Microwave Resonator Device. *Nanoscale* **2018,** 10, 4482-4889.

(60) Tang, H.; Prasad, K.; Sanjinès, R.; Schmid, P. E.; Lévy, F. Electrical and Optical Properties of TiO_2 Anatase Thin Films. *J. Appl. Phys.* **1994**, *75* (4), 2042–2047.

(61) Munuera, G.; González-Elipe, A. R.; Soria, J.; Sanz, J. Photo-Adsorption and Photo-Desorption of Oxygen on Highly Hydroxylated TiO2 Surfaces. Part 3.—Role of H2O2 in Photo-Desorption of O2. *J. Chem. Soc. Faraday Trans. 1 Phys. Chem. Condens. Phases* **1980**, *76* (0), 1535-1546.

(62) Akira Yamakata; Taka-aki Ishibashi, * and; Onishi, H. Water- and Oxygen-Induced Decay Kinetics of Photogenerated Electrons in TiO2 and Pt/TiO2: A Time-Resolved Infrared Absorption Study. **2001**, 105(30), 7258-7262

(63) Lampert, M. A.; Mark, P. *Current Injection in Solids*; Academic Press, 1970.

(64) Kang, Q.; Cao, J.; Zhang, Y.; Liu, L.; Xu, H.; Ye, J. Reduced TiO2 Nanotube Arrays for Photoelectrochemical Water Splitting. *J. Mater. Chem. A* **2013**, *1* (18), 5766-5774.

(65) Guo, Z.; Prezhdo, O. V.; Hou, T.; Chen, X.; Lee, S.-T.; Li, Y. Fast Energy Relaxation by Trap States Decreases Electron Mobility in TiO_2 Nanotubes: Time-Domain Ab Initio Analysis. *J. Phys. Chem. Lett.* **2014**, *5* (10), 1642–1647.

(66) Zarifi, M. H.; Farsinezhad, S.; Abdolrazzaghi, M.; Daneshmand, M.; Shankar, K. Selective Microwave Sensors Exploiting the Interaction of Analytes with Trap States in TiO $_2$ Nanotube Arrays. *Nanoscale* **2016**, *8* (14), 7466–7473.

(67) Zarifi, M. H.; Farsinezhad, S.; Wiltshire, B.D.; Abdorrazaghi, M.; Mahdi, N.; Kar, P.; Daneshmand, M.; Shankar, K. Effect of phosphonate monolayer adsorbate on the microwave photoresponse of TiO2 nanotube membranes mounted on a planar double ring resonator. Nanotechnology **2016**, 27 (37), Art. No. 375201.

Figures

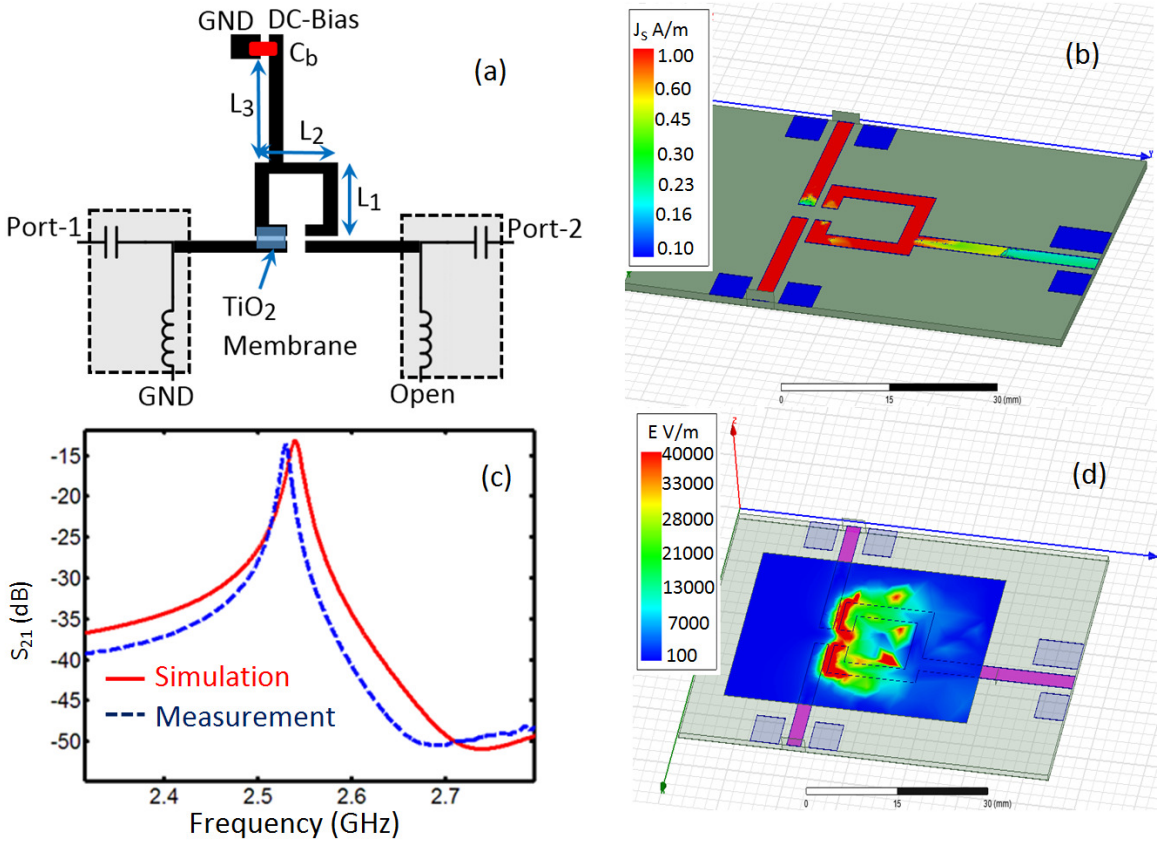

Figure 1 (a) Schematic illustration of the microwave resonator with DC bias line and a bias-Tee at each port. The width and thickness of microstrip line are 2.4 mm and 0.035 mm respectively, L_1 = 15.3 mm, L_2 = 13.8 mm, L_3 = 21.3 mm, C_b = 20 pF (b) surface magnetic current simulation to demonstrate the current path (c) resonant

profile and comparison between measured and simulated results and (d) electric field simulation to extract the most permittivity-sensitive regions of the device.

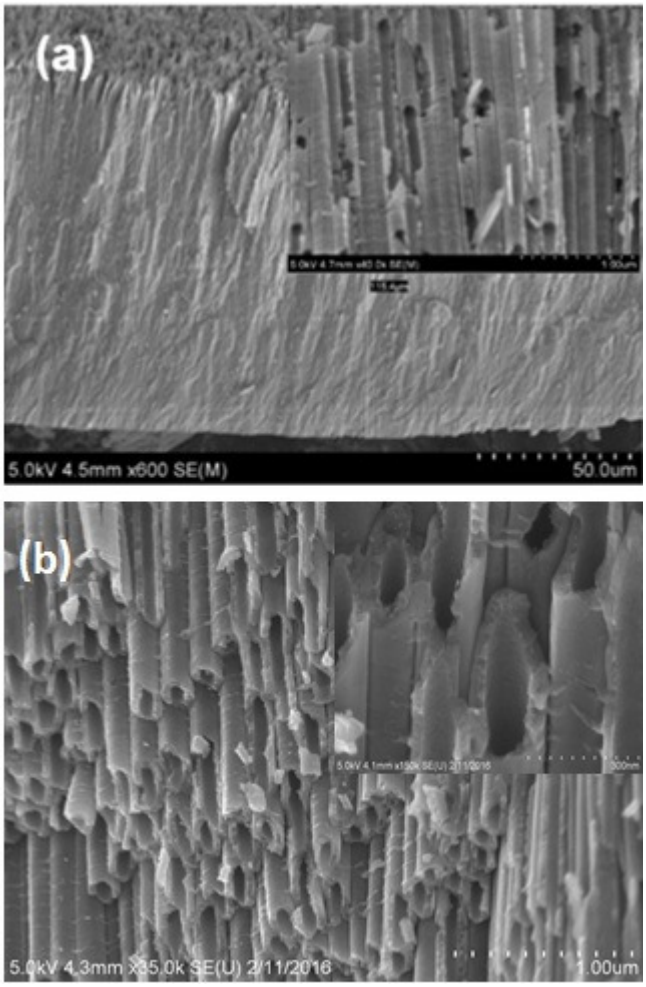

Figure 2 (a) and (b) FESEM images of the cross-section and profile view of the freestanding TNT membrane; the thickness of the membrane was measured to be 115 µm and the estimated average diameter was 125 nm.

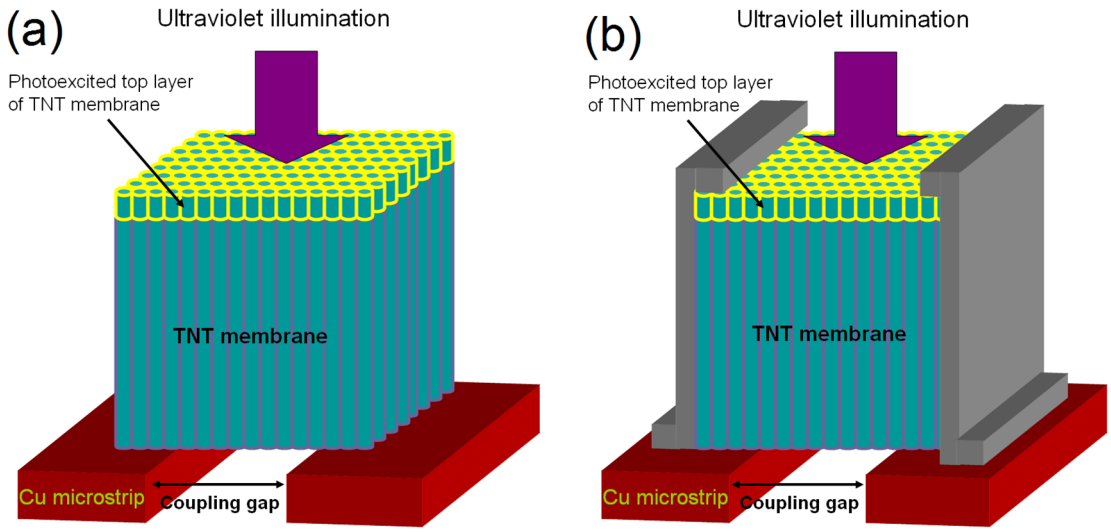

Figure 3. (a) and (b) show two slight different configurations for measuring the microwave photoresponse of free-standing TNT membranes mounted in the coupling gap of open loop split ring resonators.

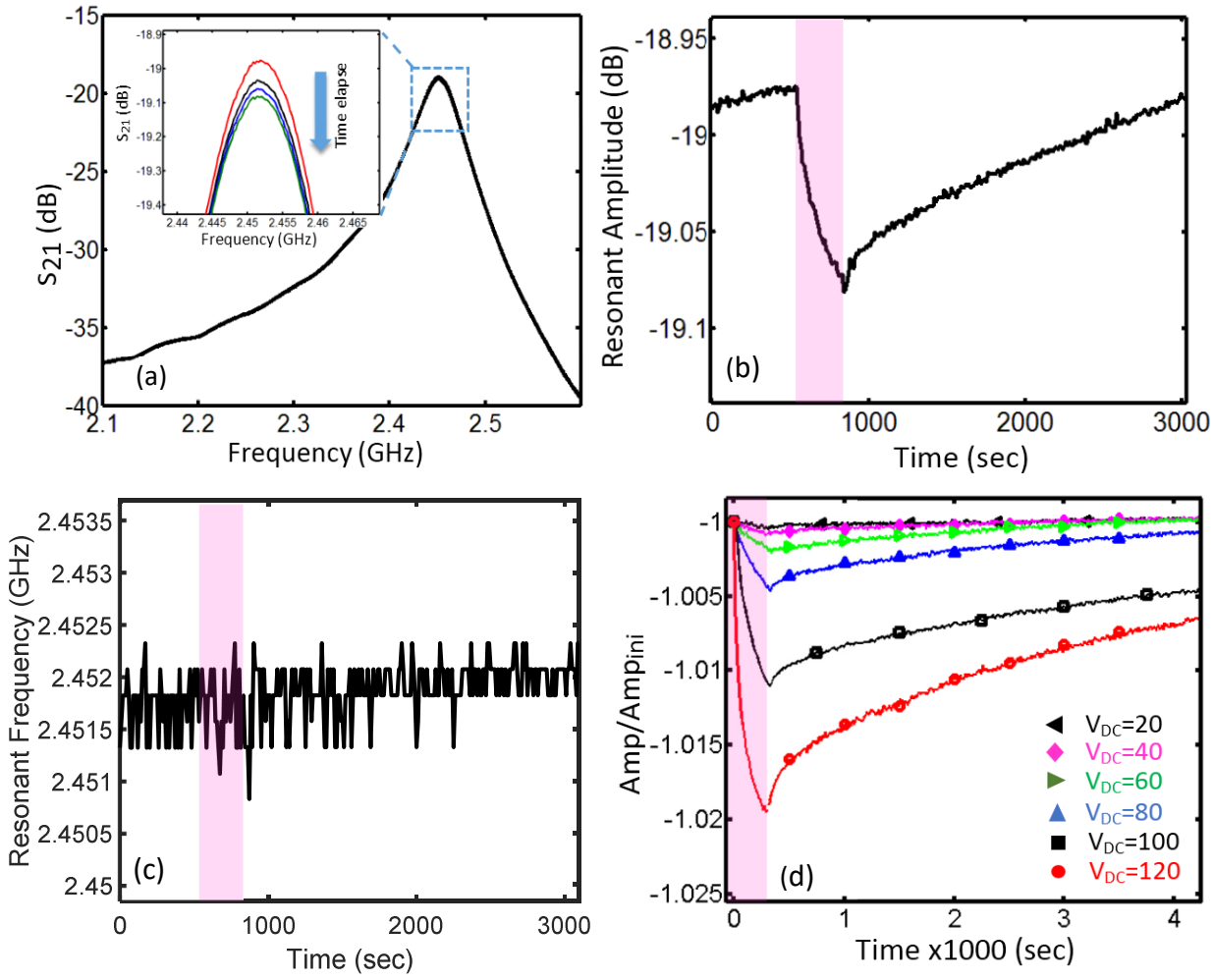

Figure 4. (a) Resonant profile of the sensor, S_{21} transmission profile is changed as time elapsed while a DC voltage of 80 V is applied (b) Resonant amplitude profile variation versus time for 5 minutes of 80V DC voltage and its relaxation (c) Resonant profile demonstrates no change while the DC voltage is applied and (d) Normalized resonant amplitude variation versus time for different DC bias voltages.

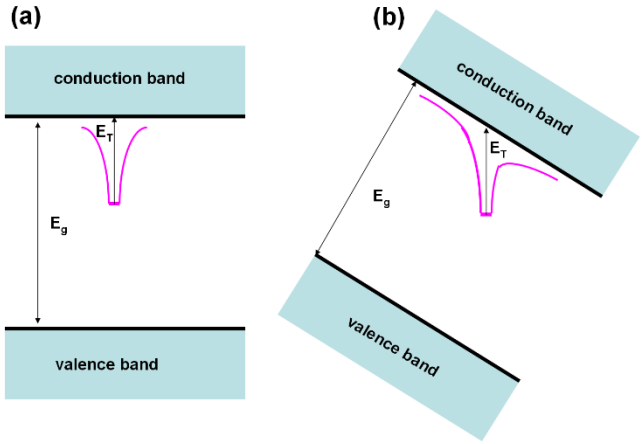

Figure 5. Energy band diagrams of a semiconductor containing a single deep level trap in the absence of an electric field (a) and in the presence of a strong electric field (b) showing the field-induced lowering in the barrier for trap emission.

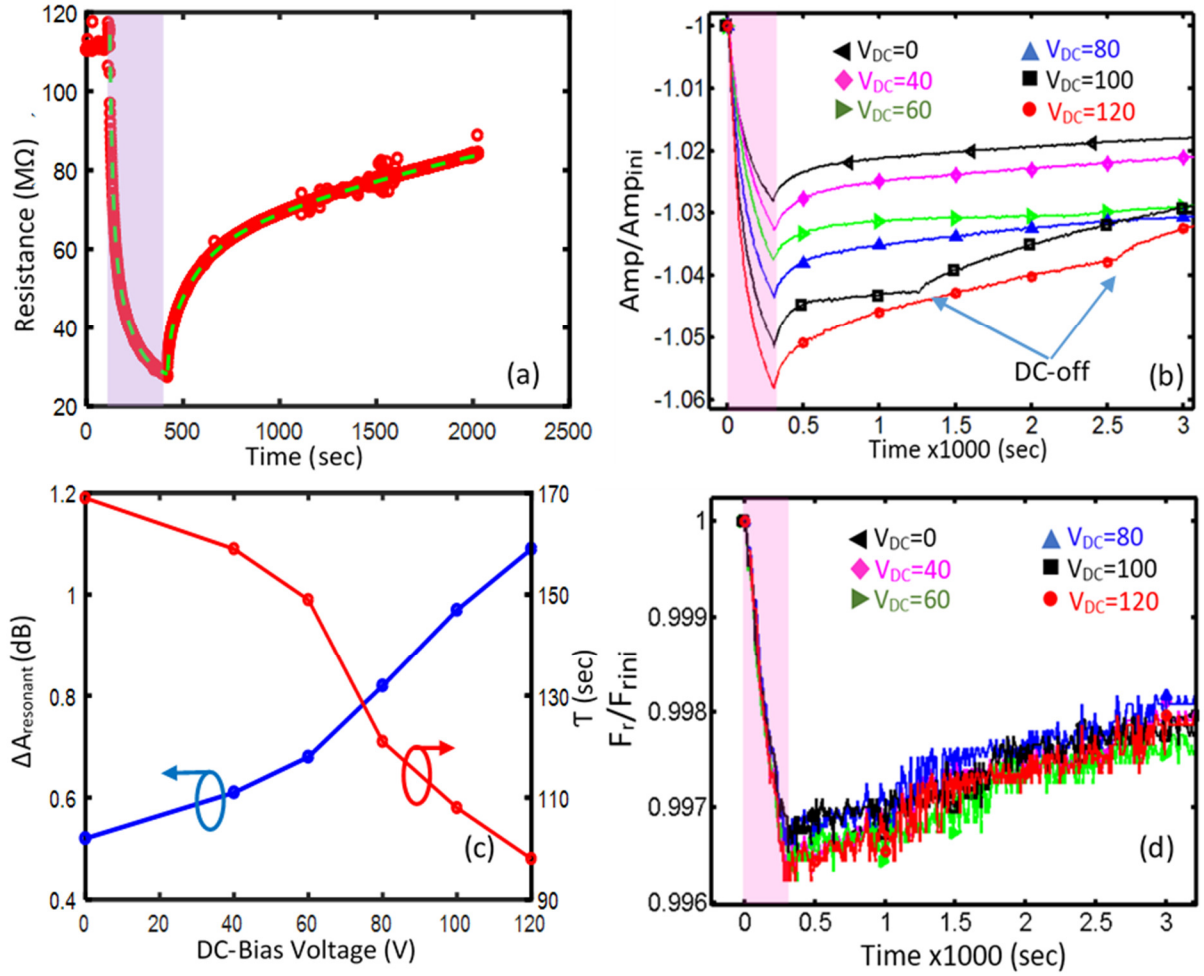

Figure 6. (a) Resistivity variation from 110 to 30 MΩ during the 5-minute UV-illumination on the glued TiO_2 nanotube membrane, (b) transient response of the UV-illuminated membrane regarding to the different applied DC-bias voltages, (c) amplitude and time constant of the resonant amplitude behavior versus applied bias voltage in presence of UV illumination, (d) Resonant frequency variation during the UV-illumination and the resting period regarding to different bias voltages.

TOC (**Graphical Abstract**)